Impact of the Oxygen Vacancies of the LSCF (La$_{0.6}$Sr$_{0.4}$Co$_{0.2}$Fe$_{0.8}$O$_{3−δ}$) Perovskite on the Activation Energy of the Oxygen Reduction/Evolution Reaction

Paola Costamagna, Caterina Sanna, Peter Holtappels, Cristina Artini,* and Marcella Pani

La$_{0.6}$Sr$_{0.4}$Co$_{0.2}$Fe$_{0.8}$O$_{3−δ}$ (LSCF) perovskites, in the form of in–house electrospun nanofibers and commercial powders, have been tested through synchrotron x–ray diffraction and electrochemical impedance spectroscopy in the 800–1200 K range. The former analyses make it possible to evaluate the oxygen vacancies (OV) concentration, and the latter allows to assess the electrokinetics of the oxygen reduction/evolution reaction. Equivalent circuit modeling is carried out to identify the basic electrochemical processes and evaluate the associated polarization resistance R_p. One high-frequency process and two intermediate-frequency processes are recognized. For all electrochemical processes, OV concentration and R_p behave similarly with temperature in both nanofiber and granular electrodes. This led to the proposal of a new equation. For each electrochemical process, it was shown that the activation energy is the sum of an intrinsic electrochemical activation energy, plus the formation energy of OVs. For the LSCF perovskites tested in this work, the intrinsic electrochemical activation energy was found to be independent of the preparation procedure and crystal structure. In contrast, the OV formation energy was found to be strongly dependent on the preparation procedure and crystal structure, with values ranging between 0.5 and 24.1 kJ mol$^{−1}$. A complete set of data is provided, which can be useful for future simulation studies.

1. Introduction

The oxygen reduction reaction (ORR) is the electrochemical reaction occurring at the air side of electrochemical cells for energy conversion and storage, such as fuel cells and metal–air batteries, whereas the reverse reaction, namely the oxygen evolution reaction (OER), occurs in electrolysis operation mode. In both cases, the slowness of the kinetics is a limiting factor,

P. Costamagna, C. Sanna,[+] C. Artini, M. Pani
DCCI, Department of Chemistry and Industrial Chemistry
University of Genoa
Via Dodecaneso 31, I–16146 Genoa, Italy
E-mail: artini@chimica.unige.it

P. Holtappels[++]
DTU Energy
Technical University of Denmark
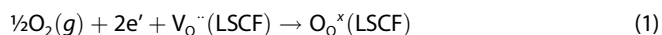*Elektrovej 375, DK–2800 Kgs. Lyngby, Denmark*

C. Artini
CNR–ICMATE
Italian National Research Council
Via De Marini 6, I–16149 Genoa, Italy

M. Pani
CNR–SPIN
Italian National Research Council
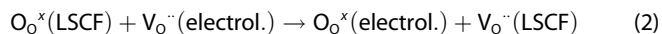*Corso Perrone 24, I–16152 Genoa, Italy*

[+]*Present address: ERG, Via de Marini 1, I–16149 Genoa, Italy*

[++]*Present address: IMVT, Institute for Micro Process Engineering, Karlsruhe Institute of Technology (KIT), Hermann–von–Helmholtz–Platz 1, D–76344 Eggenstein–Leopoldshafen, Germany*

which strongly affects performance. Among the possible materials to be used as electrocatalysts for ORR/OER, ABO$_3$ perovskite oxides are now intensively studied, mainly due to their high electrocatalytic activity, which has been proposed to be largely related to the presence of oxygen vacancies (OVs) in the crystal lattice.[1]

Within the family of ABO$_3$ perovskite oxides, the La$_{0.6}$Sr$_{0.4}$Co$_{0.2}$Fe$_{0.8}$O$_{3−δ}$ (LSCF) perovskite is the state-of-the-art air electrode for intermediate temperature–solid oxide fuel cells (IT–SOFCs) and solid oxide electrolysis cells (SOECs).[2]

It is well known that LSCF crystallizes in two different structures, according to temperature and composition, namely in the ideal cubic one (space group: $Pm\bar{3}m$) or in the rhombohedral one, belonging to the $R\bar{3}c$ space group.[3,4] While in the former the BO$_6$ octahedra are regular,[1] in the latter, which is one of the most commonly occurring structural distortion of perovskite, they are strongly tilted.[3,4] The perovskite structure is indeed highly flexible, and as a consequence, oxygen atoms can leave the lattice, creating OVs, without causing structural collapse. In the framework of the optimization of electrode materials, the role of OVs is of primary importance, being they responsible of peculiar physical and chemical properties, including mixed ionic–electronic conducting (MIEC) behavior, and electrocatalytic activity toward the ORR/OER.[1] On one hand, C_{OV} influences in fact the ionic conductivity of LSCF, thus affecting the electrochemical performance of LSCF. On the other hand, oxygen vacancies take part directly in electrochemical reactions. Many different mechanisms have been proposed, which can basically be simplified as the overlapping of a surface path and a bulk path.[5] These are usually expressed through the Kröger–Vink notation. For example, referring to the ORR reaction, the surface path is as follows[5]

$$\tfrac{1}{2}O_2(g) + 2e' + V_O^{\cdot\cdot}(LSCF) \rightarrow O_O^x(LSCF) \tag{1}$$

Bulk path:

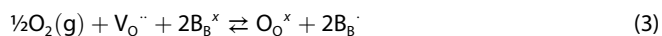$$O_O^x(LSCF) + V_O^{\cdot\cdot}(electrol.) \rightarrow O_O^x(electrol.) + V_O^{\cdot\cdot}(LSCF) \tag{2}$$

According to this, an increase of C_{OV} in LSCF should enhance the kinetics of the surface path, leading to an increased concentration of oxygen ions in the bulk of LSCF. This, in turn, should enhance the kinetics of the bulk path, leading to an overall increase in the electrochemical performance.

Moreover, the ORR/OER is strongly influenced by the OVs formed at the perovskite surface, and it has been demonstrated that nanostructuring methods, enhancing the surface area, have the potential to improve ORR/OER kinetics by promoting OV formation.[6] The key role of OVs in the ORR/OER kinetics has been demonstrated also for Ruddlesden–Popper perovskites ($A_{n+1}B_nO_{3n+1}$), a layered derivative of the perovskite family (ABO_3), which are emerging as high-performing electrocatalysts.[7]

The evaluation of the OV concentration (C_{OV}) is a crucial point in the study of LSCF.[8–10] It was pointed out that OV formation is associated with an oxygen equilibrium between the solid oxide and the gas atmosphere. This can be described by the following defect equilibria (in Kröger–Vink notation)

$$\tfrac{1}{2}O_2(g) + V_O^{\cdot\cdot} + 2B_B^x \rightleftarrows O_O^x + 2B_B^{\cdot} \tag{3}$$

$$2B_B^x \rightleftarrows B_B' + B_B^{\cdot} \tag{4}$$

where all the species are in the LSCF crystal structure (except for molecular oxygen, in the gas phase). Furthermore, B = Co and Fe. Reaction (3) describes the oxygen exchange between solid and gas phase via the annihilation of OVs and oxidation of B^{3+} to B^{4+}. Reaction (4) represents the charge disproportionation of B^{3+} into B^{4+} and B^{2+}. Defect chemical modeling was performed applying an ideal solution model. The model was fitted to thermogravimetry experimental data with temperature from 976 to 1176 K and pO_2 from 1E−5 to 1 atm. In this way, the standard enthalpy and entropy of oxidation (3) and charge disproportionation (4) reactions were evaluated. It was found that, for $La_{0.4}Sr_{0.6}Co_{1-y}Fe_yO_{3-\delta}$, with $0 \le y \le 1$, $\Delta H^\theta_{(3)} = (-91 \pm 15)$ kJ (mol O)$^{-1}$. For Reaction (4), $\Delta H^\theta_{(4)} = 22 \pm 20$ kJ (mol O)$^{-1}$ for $y = 0$, and 134 ± 66 kJ (mol O)$^{-1}$ for $y = 1$.[9] Anyway, in the same works it was pointed out that, in the materials under investigation, the concentration of defects was well above the applicability limits of the ideal solution model.[8–10] Therefore, more in-depth studies were deemed necessary. For example, a subsequent study proposed three versions of point defect chemistry models. The models were fitted to thermogravimetric experimental data.[11] It was found that only by increasing the model complexity and the number of fitting parameters was it possible to obtain excellent reproduction of the experimental data. Further in this direction, ab initio calculations performed using density functional theory (DFT)[12–14] provided results which were fitted to oxygen permeation experimental data in the temperature range 1073 to 1273 K. For $La_{0.98-x}Sr_xCo_{0.2}Fe_{0.8}O_{3-\delta}$, with $0.125 \le x \le 0.8$, $\Delta H^\theta_{(3)}$ was evaluated, obtaining results in agreement with those reported above.[9,14]

Nevertheless, most of the aforementioned studies focused on temperatures higher than those currently considered for IT-SOFCs and SOECs,[8–10,12–14] highlighting the need for further investigation in the temperature range 800–1100 K. Furthermore, the effect of the LSCF preparation route and structural transition on C_{OV} was not explored either. Finally, no attempts have been made to demonstrate a correlation between C_{OV} and ORR/OER kinetics.

The most common technique for measuring electrochemical kinetics is electrochemical impedance spectroscopy (EIS).[15] This technique, combined with equivalent circuit modeling (ECM), makes it possible to identify basic electrochemical processes and to evaluate the associated polarization resistance R_p. The overall polarization resistance of the electrode $R_{p,TOT}$ and its activation energy E_a can also be evaluated. Interestingly, a wide distribution of E_a values has been reported in the literature for LSCF electrodes.[16] In contrast, it has been observed that LSCF electrodes prepared by electrospinning show highly reproducible E_a values.[16–18] This suggests that the ORR/OER kinetics is influenced by electrode morphology and preparation route.

The impact of electrode morphology and preparation route on the structural and electrocatalytic features of LSCF was studied in a previous work.[19] To this purpose, LSCF was studied in two different forms: in-house electrospun nanofibers and commercial granular powders, with the latter used as control sample. Based on high-temperature synchrotron X-ray diffraction (XRD), morphology in fact significantly affects the structural properties of LSCF. In particular, LSCF nanofibers prepared through the electrospinning technique assume a rhombohedral (R) structure throughout the whole temperature range investigated, namely from room temperature up to 1200 K. Instead, the commercial LSCF powders, tested in the same temperature range, exhibit the R structure at low temperature and the cubic (C) structure at high temperature, with the R → C transition occurring at about 1023 K. Other structural differences were clearly detected in the cell volume, higher in the nanofibers; in the thermal expansion coefficient, of lower magnitude in the nanofibers; in the oxygen vacancy concentration and in the microstrain, both higher in nanofibers than in powders, with discontinuities of these last two properties in granular samples at the temperature of the structural transition. Correspondingly, a discontinuity was found in the Arrhenius plot of the polarization resistance R_p of the powders, whereas no discontinuity was found in nanofibers.[19]

In the present work, the correlation between C_{OV} and ORR/OER kinetics is analyzed in more detail, focusing on the role of the electrode morphology on the crystal structure, and hence on the OV amount. With the aim to find a key to understand the differences between the electrochemical behavior of LSCF nanofibers and powders, OV concentration obtained from high-temperature synchrotron XRD experiments and ORR/OER experimental data obtained from EIS performed at open-circuit voltage (OCV) are correlated, and a relationship between the formation energy of OVs, $E_{a,OV}$, and the activation energy of the ORR/OER, E_a, is proposed.

2. Results

2.1. Oxygen Vacancies

More details on the high temperature synchrotron experiments and the complete set of experimental XRD data is given in a previous work,[19] whereas a summary of the main results can be found in the final part of the Introduction. Here, OVs in nanofiber and granular LSCF are evaluated on the basis of XRD data, following the procedure described in the Experimental Section of this paper. **Figure 1**a reports the percentage of OVs in the crystal lattice as a function of temperature, in the temperature range under study for IT–SOFCs (800–1200 K). Overall, OVs increase with increasing temperature, and this is in agreement with previous literature results.[9] For nanofibers, which retain the R structure throughout the whole temperature range, the increase of oxygen vacancies is linear and continuous. Instead, for granular powders, the results show a discontinuity and an abrupt increase at the $R \rightarrow C$ transition. Below the $R \rightarrow C$ transition temperature, the OV percentage is superior in nanofibers, whereas above the $R \rightarrow C$ transition the situation is reversed.

Figure 1b shows an Arrhenius plot of the OV concentration, C_{OV}. Data are fitted through Arrhenius lines, and the obtained activation energies $E_{a,OV}$ are the formation energies of OVs. Values of $E_{a,OV}$ are 2.8 kJ mol^{-1} for nanofibers throughout the whole temperature range, 24.1 kJ mol^{-1} for powders at temperatures below the $R \rightarrow C$ transition, and 0.5 kJ mol^{-1} for powders at temperatures above the $R \rightarrow C$ transition. Therefore, data in Figure 1b demonstrate that both the preparation procedure and the crystal structure strongly influence $E_{a,OV}$, which is a substantial novelty compared to previous works.[9,12,14] In principle, when considering different LSCF samples with the same chemical composition, the variation in OV concentration should follow a thermodynamic relationship with temperature and oxygen partial pressure of the atmosphere. Therefore, in a thermodynamic view, OV concentration should not be changed by material morphology. Nevertheless, in nanostructured perovskites, where the surface effects are dominating, this may be no more true. In a review work on nanostructuring methods for perovskite electrocatalysts, the higher C_{OV} close to the surface of the nanostructure

elements is suggested to promote the ORR.[6] This is in agreement with DFT studies, demonstrating that the overall chemical composition has only a small impact, whereas the main factor is the local cation configuration which affects the charge redistributions and transition state energies during the oxygen migration associated to the formation of OVs.[12] Therefore, near the surface of the nanostructure elements, the local energy profiles are expected to be different from those in the bulk, and this may explain the dependence of OV concentration C_{OV} and activation energy $E_{a,OV}$ on the preparation procedure.

The values obtained for $E_{a,OV}$ may be not valid outside the investigated temperature range. In particular, excessive OV concentration occurring at extremely high temperatures may harm the structural stability, with possible subsequent structural collapse in favor of a more stable atomic arrangement.[1]

2.2. Oxygen Reduction/Evolution Reaction

Figure 2 reports the Nyquist plots of EIS experimental data of LSCF nanofiber and powder electrodes, tested at 923 K. A full set of EIS experimental data for temperatures spanning from 823 up to 1223 K is reported in previous works.[17,19] In Figure 2, fittings performed through the ECM technique are also shown, as well as the individual contributions of the elements of the equivalent circuit (EC). More details about the EC can be found in the Experimental Section. In particular, the electrode structure and the physical meaning proposed for the EC elements are schematized in Figure 5.

Comparing Figure 2a,b, the first observation is that the high frequency intercept of the impedance arcs with the real axis assumes the same value. This is the resistance associated with the transfer of the oxygen ions through the electrolyte, corresponding to the Rs element of the EC. Since the electrolyte is identical in both cases, Rs is also the same (around 0.53 Ω cm^2). Apart from this, the shape of the two impedance arcs is remarkably different. In fact, the LSCF nanofibers (Figure 2a) exhibit an almost pure Gerischer arc, with nearly negligible depression.[17] Instead, the granular powders (Figure 2b) display two main arcs with markedly depressed RQ behavior. According to previous studies, these differences are due to the different electrode
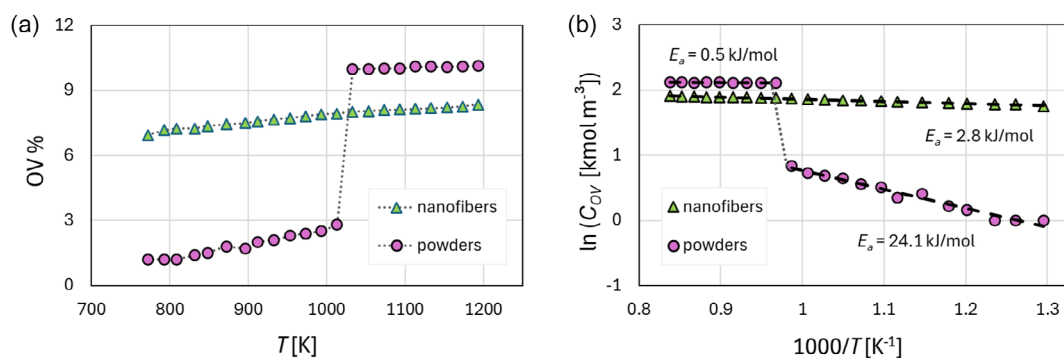

Figure 1. Oxygen vacancies (OVs) as a function of temperature in LSCF nanofibers and powders: a) OV% and b) OV concentration C_{OV}. Dotted lines join adjacent data. Dashed lines are linear fittings, reported together with the corresponding activation energies, $E_{a,OV}$.
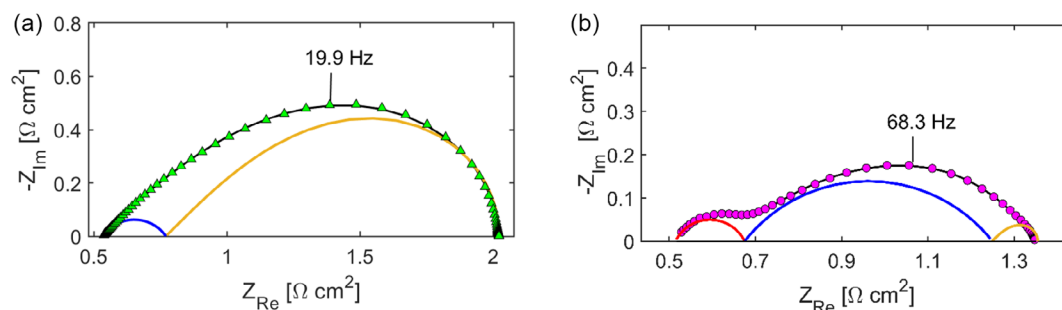
ChemElectroChem

Research Article
doi.org/10.1002/celc.202500165

**Chemistry
Europe**

European Chemical
Societies Publishing

Figure 2. Nyquist plots of EIS experimental data (symbols) and ECM fittings (black lines) of LSCF electrodes at 923 K: a) nanofibers and b) granular powders. The impedances of the individual EC elements are represented as well: RQ1 (red line), RQ2 (blue line), G (yellow line).

morphologies, and in particular to the long path of the electrical charges along the nanofibers, and the short path along the granules of the powders.[19] Nanofibers have a length of several micrometers and a cross-sectional diameter of approximately 0.2 μm.[19] There, distributed electrochemical reaction occurs along with charge conduction, and this explains the prevailing Gerischer (G) impedance clearly visible in Figure 2a). Furthermore, the small number of fiber–fiber contacts gives a small RQ response (RQ2 circuit element). Since the fibers adjacent to the electrolyte lay and adhere onto it, their interface gives negligible RQ response (RQ1 circuit element). Instead, with powders (Figure 2b), the path along the powder grains is short in length (granule diameter 0.9 μm) and has a large cross-section (again related to granule diameter 0.9 μm), resulting in a reduced

G impedance.[19] Instead, the numerous grain–grain contacts, acting as electrochemical interfaces, give a prevailing RQ2 response (the main impedance arc). Depression, clearly visible in this case, is usually associated with highly distributed interfaces. Finally, the small powder grain–electrolyte contacts cause a significant high-frequency RQ1 impedance, clearly visible in this case.

Figure 3 reports the total polarization resistance $R_{p,TOT}$ and the polarization resistances associated to the different EC elements $R_{p,RQ1}$, $R_{p,RQ2}$, and $R_{p,G}$. The data are shown in Arrhenius plots of reciprocal polarization as a function of $1000\,T^{-1}$. Data of the nanofiber electrode are well fitted by an Arrhenius line and show no change in slope. With regard to powder electrodes, a comparison was made between the fit of the experimental data to a single straight line and two separate straight lines. The results
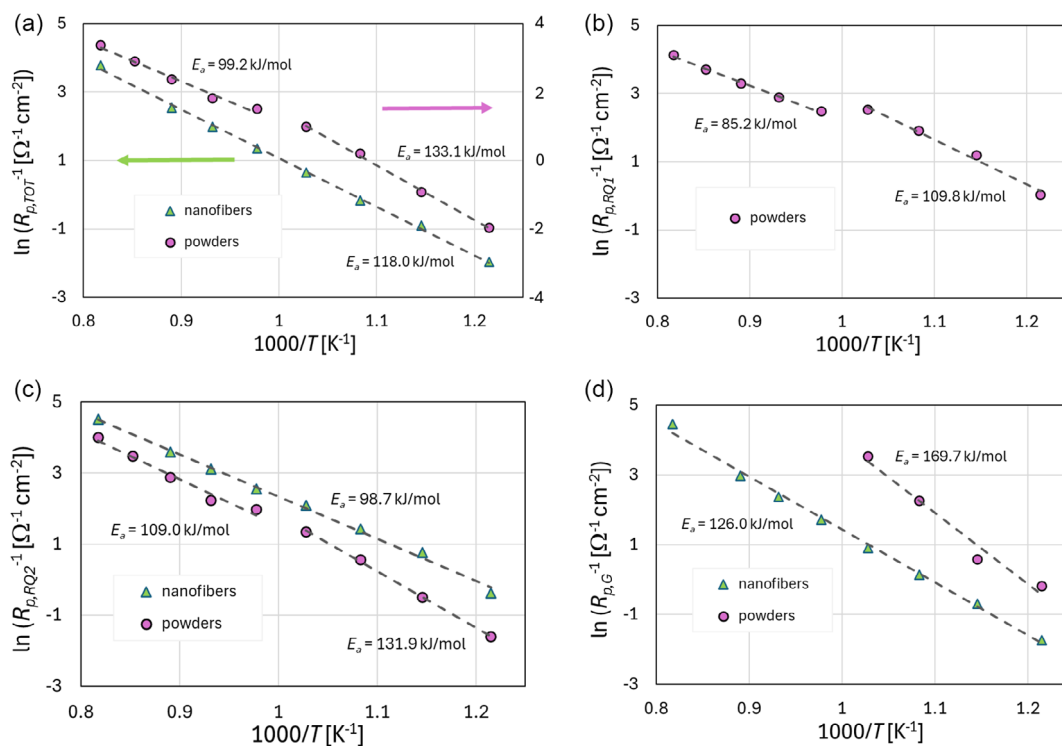

Figure 3. Arrhenius plot of R_p^{-1} and the contributions associated with the different elements of the EC: a) $R_{p,TOT}^{-1}$, b) $R_{p,RQ1}^{-1}$, c) $R_{p,RQ2}^{-1}$, and d) $R_{p,G}^{-1}$. Symbols are values derived from the EIS experimental data, and dashed lines are linear fittings, reported together with the corresponding activation energies E_a.

ChemElectroChem

Research Article
doi.org/10.1002/celc.202500165

**Chemistry
Europe**
European Chemical
Societies Publishing

showed that, overall, the fitting with two straight lines had a better coefficient of determination R^2. This means that there is a change in slope, that is, a change in behavior, around 1023 K, and this is consistent with the occurrence of the R → C transition.

In particular, Figure 3a compares the total polarization of nanofiber and powder electrodes. Data obtained from the two electrodes are very close to each other. Regarding powder electrodes, the slope of the Arrhenius fitting line is higher at low temperatures (R structure) rather than at high temperatures (C structure). In other words, the activation energy E_a is higher at low than at high temperatures. This is similar to the Arrhenius plot of the OV concentration, C_{OV}, reported in Figure 1b. This suggests a correlation between E_a and $E_{a,OV}$. From a physical-chemical point of view, this can be explained supposing that the increase in $R_{p,TOT}^{-1}$ with temperature originates not only from the activation of the electrochemical processes, but also from the increase of vacancy concentration with temperature.

These results are also confirmed by the behavior of the R_p^{-1} associated to all the individual elements of the EC. The results regarding the polarization resistance of the RQ1 element are reported in Figure 3b, only for the powder electrode since, as already remarked, the RQ1 impedance is zero in nanofiber LSCF electrodes. Figure 3b shows that, at the R → C transition $R_{p,RQ1}$ has a marked discontinuity and a slope change. Also here, the slope is greater at low than at high temperatures. The fact that the RQ1 term is clearly affected by the R → C transition occurring in the LSCF confirms that this high-frequency process is also related to the features of the electrode and not only those of the electrolyte (i.e., grain boundaries), as claimed by several works.[20] This supports the hypothesis that RQ1 represents the impedance of the interface between the electrolyte and the adjacent granules.[21] Another remark is that, when increasing temperature across the R → C transition, an improvement of performance may be expected on the basis of the increase of OVs shown in Figure 1. Instead, Figure 3b shows a decrease in performance, which may be ascribed to a distortion of the electrochemical interface due to the change in LSCF crystal structure.

Figure 3c shows the R_p^{-1} associated with the RQ2 element. The $R_{p,RQ2}^{-1}$ is larger in the nanofiber than in the powder electrode, in agreement with the results reported in Figure 2. Here, the discontinuity in the powder electrode data is less marked than in RQ1, but still appreciable. Again, the slopes of the Arrhenius lines confirm the behavior in Figure 3a.

Finally, Figure 3d shows the R_p^{-1} of the G element. In this case, the $R_{p,G}^{-1}$ of the nanofiber electrode is smaller than for the powder electrode, in agreement with the results reported in Figure 2. The slopes of all the Arrhenius lines are higher than for the RQ1 and RQ2 elements, demonstrating the boosting effect of temperature on the ORR/OER electrokinetic rate within the LSCF perovskite. Regarding the powder electrode, the impedance of the G element vanishes above the R → C transition. This indicates that the boosting effect of temperature is even greater in the stability range of the cubic crystal structure. Also in this case, nanofibers do not show any discontinuity nor change in slope throughout the whole range.

The activation energies of the R_p^{-1} of all the EC elements are summarized in **Table 1**. For sake of completeness, the pre-exponential factors are reported in **Table 2**.

Figure 4 reports the values of the ECM fitting parameters. Figure 4a shows the values of α, the exponent of the CPE elements embedded into the RQ elements, according to Equation (17). The value of α is associated to the broadness of the distribution across the electrochemical interface: α = 1 is related to an ideal capacitor (no distribution), and α < 1 is associated to a distributed phenomenon. The broader the distribution, the lower the value of α; usually 0.8 < α < 1.[15] Figure 4a shows the values of α for the RQ1 element of the EC only for powder electrodes, because the RQ1 element is ideal for nanofiber electrodes, that is, its impedance is zero. In addition, Figure 4a shows the values of α for the RQ2 element of the EC for both nanofiber and powder electrodes. All the α values in Figure 4a are similar and exhibit a moderate variation in the temperature range between 873 and 1073 K, with α taking rather small values ranging between 0.5 and 0.7. These values are consistent with highly distributed processes at the nanoscale (nm) of the interfaces, which are highly nonuniform. Toward the ends of the operating temperature range, the values of α show a noticeable increase which can be attributed to a shrinkage of the thickness where the electrochemical reaction occurs across the electrolyte–electrode and intraparticle interfaces. The only exception is the value of α of the RQ1 element in the powder electrode, which has a value as low as α = 0.32 at 823 K. This can be explained in terms of poor contact between the electrolyte and the LSCF granules, which is only visible at low temperatures where it is not compensated by thermal expansion. A final comment is that the profile of α is rather regular for the nanofiber electrode, whereas both α profiles of the powder electrode show a negative spike at temperatures close to the R → C transition.

Figure 4b shows the equivalent area-specific capacitance $Q_{equiv.}$, calculated according to Equation (18). For the powder electrode, the values of $Q_{equiv.}$ of RQ1 are in the range

Table 1. Activation energies E_a (in [kJ mol^{-1}]) of the R_p^{-1} of the EC elements.

	Fibers	Powders $T < T_{R \to C \text{ transition}}$	Powders $T > T_{R \to C \text{ transition}}$
$R_{p,TOT}^{-1}$	118.0	133.1	99.2
$R_{p,RQ1}^{-1}$	–	109.8	85.2
$R_{p,RQ2}^{-1}$	98.7	131.9	109.0
$R_{p,G}^{-1}$	126.0	169.7	–

Table 2. Pre-exponential factors k_0'' of the R_p^{-1} of the EC elements Equation (12). Values to be multiplied for 10^6 [Ω^{-1} cm^{-2}].

	Fibers	Powders $T < T_{R \to C \text{ transition}}$	Powders $T > T_{R \to C \text{ transition}}$
$R_{p,TOT}^{-1}$	4.248	38.764	0.467
$R_{p,RQ1}^{-1}$	–	10.639	0.256
$R_{p,RQ2}^{-1}$	14.500	48.014	2.278
$R_{p,G}^{-1}$	16.159	37 891.8	–

ChemElectroChem

Research Article
doi.org/10.1002/celc.202500165

**Chemistry
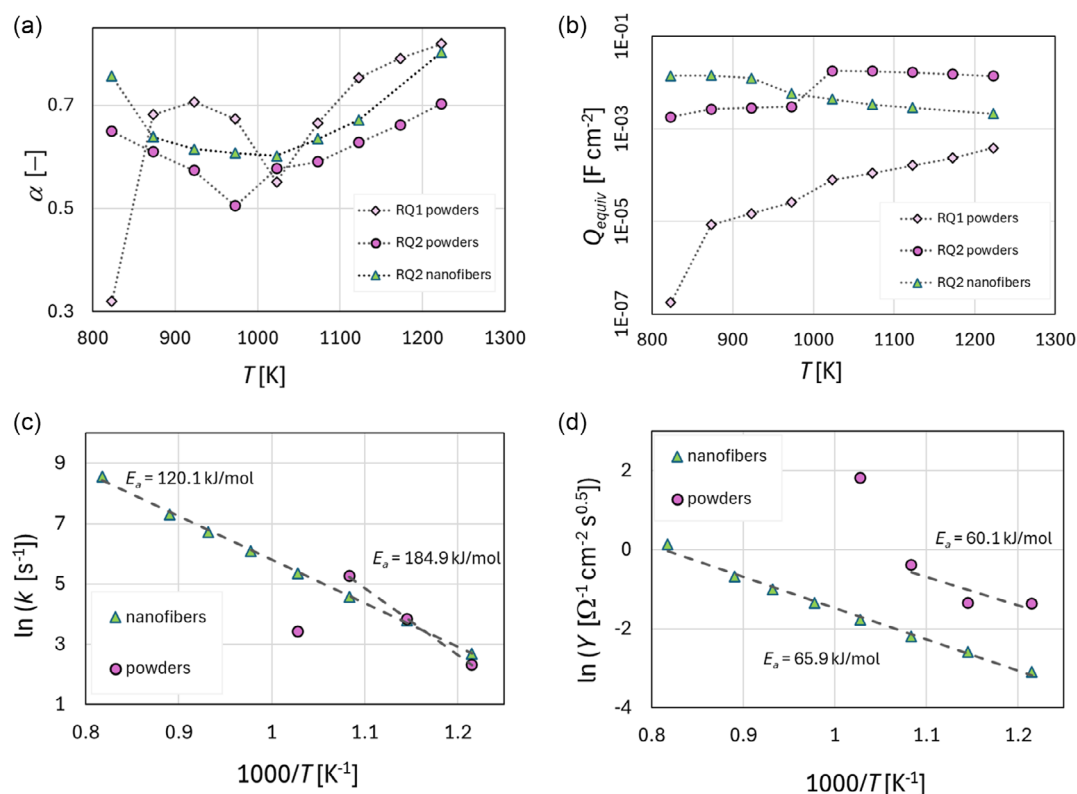Europe**

European Chemical
Societies Publishing

Figure 4. Values of the ECM fitting parameters. RQ1 and RQ2 circuit elements: a) exponent α in Equation (17) and b) equivalent capacitance $Q_{equiv.}$ in Equation (18). Gerischer element: c) oxygen surface exchange coefficient k and d) admittance Y, both in Equation (19). Dotted lines join adjacent data. Dashed lines are linear fittings, reported together with the corresponding activation energies E_a.

10^{-6}–10^{-3} F cm^{-2}. The process underlying RQ1 is a high-frequency one, with summit frequency $f_{max} \approx 10^5$ Hz, almost independent of temperature. Again, these data confirm the attribution to a charge transfer process at the electrode/electrolyte interface.[22] Regarding the RQ2 element, the equivalent capacitance is in the range 10^{-3}–10^{-1} F cm^{-2} for both the nanofiber and the granular electrode. These capacitances are of the same order of magnitude as those reported in the literature for intermediate-frequency processes in LSCF electrodes.[23] The summit frequency confirms the intermediate-frequency nature of the RQ process, being $f_{max} \approx 10^1$ to 10^3 Hz at temperatures between 823 and 1223 K. These data are practically identical for both the nanofiber and powder electrodes, and therefore, it is evident that RQ2 is the same process in both electrodes. The literature attributes these intermediate-frequency processes to several possible phenomena, including interfacial charge transfer (not involving the electrolyte).[23,24] A final comment is that the profile of $Q_{equiv.}$ of the RQ2 element is rather regular for the nanofiber electrode, whereas the powder electrode shows an abrupt increase at the R $\rightarrow$ C transition.

Figure 4c,d shows the fitting values of the parameters k and Y of the Gerischer element, appearing in Equation (19). The data are presented in an Arrhenius plot. Fitting is performed and activation energies E_a are calculated. The data for the powder electrode present some scatter due to the intrinsic difficulties of fitting a small arc (G) adjacent to other large arcs (RQ1 and RQ2), as

depicted in Figure 2b. In particular, the k and Y values at 973 K are not in line with the others, possibly due to the impending crystal structure transition. Therefore, the values at 973 K are excluded from the Arrhenius line fittings. Nevertheless, Figure 4c, d makes it possible to draw some considerations. The coefficient k, representing in lumped form the kinetics of the ORR/OER reaction occurring inside the LSCF material, has very similar values for nanofiber and granular electrodes. This confirms that the process is the same. Instead, the activation energies E_a are different, much higher for the powder electrodes, in agreement with the higher rate of OV formation with temperature demonstrated in Figure 1. Finally, Figure 4d shows the fitting values of the parameter Y, embedding in a lumped way structural parameters and the solid phase oxygen diffusion coefficient. Here, it is interesting to notice that the values of Y are higher for the powder rather than for the nanofiber electrode. As already remarked, the granules of the powders offer a larger cross-section and shorter paths for the oxygen transport, compared to nanofibers. This reduces the impedance and thus explains the higher Y values for the powder electrode. On the other hand, the activation energies E_a of Y are practically the same for both electrodes. Instead, a larger E_a should be expected for the powder electrode, since Y embeds also the solid phase oxygen diffusion coefficient, which should gain advantage from the superior increase of OV concentration by increasing temperature. In this case, the scattering of the powder electrode data, together with their small number,

ChemElectroChem

Research Article
doi.org/10.1002/celc.202500165

Chemistry Europe
European Chemical
Societies Publishing

makes the value calculated for E_a unreliable, and therefore, no conclusion can be drawn.

3. Discussion

Figure 3 shows the Arrhenius plot of $R_{p,TOT}^{-1}$, $R_{p,RQ1}^{-1}$, $R_{p,RQ2}^{-1}$, and $R_{p,G}^{-1}$. For powder electrodes, the slope of the Arrhenius lines is always higher at temperatures below, rather than above, the $R \rightarrow C$ transition. For nanofiber electrodes, the slope of the Arrhenius lines is always constant for the entire temperature range, and similar to that of powder electrodes above the $R \rightarrow C$ transition. The correlation with the results reported for OVs in Figure 1b is evident. This suggests analyzing the E_a, activation energies of the R_p^{-1} of the EC elements, after subtracting the corresponding $E_{a,OV}$, activation energies of OV formation. The results are reported in **Table 3**. For powder electrodes, for the EC element RQ1, the values obtained below and above the $R \rightarrow C$ transition are practically identical. An analogous result is found also for the EC element RQ2.

This suggests that, for the RQ1 and RQ2 EC elements, the overall activation energy E_a is the sum of an intrinsic activation energy $E_{a,intrinsic}$, plus the formation energy of OVs, $E_{a,OV}$

$$E_a = E_{a,intrinsic} + E_{a,OV} \tag{5}$$

To put this in a theoretical context, it must be considered that all experimental electrochemical data were obtained around the OCV and that the linear behavior of the experimental electrode was successfully verified, as reported in the Experimental Section of this paper. Therefore, the linear approximation of the Butler–Volmer equation can be applied[25,26]

$$R_p^{-1} = \frac{nF}{RT} i_0 \tag{6}$$

where n [–] is the number of electrons exchanged in the electrochemical reaction, F is the Faradays' constant [$C\,mol^{-1}$], R is the gas constant [$J\,mol^{-1}\,K^{-1}$], T is temperature [K], and i_0 is the exchange current density [$A\,m^{-2}$]. The exchange current density is the main electrokinetic parameter, which in turn, can be expressed as

$$i_0 = C_r^{v_r} C_p^{v_p} k_o \exp\left(-\frac{E_{a,intrinsic}}{RT}\right) \tag{7}$$

where C_r and C_p are reactants and products concentrations [$mol\,m^{-3}$], v_r and v_p are reactants and products reaction orders

Table 3. Activation energies $E_{a,intrinsic}$ (in [$kJ\,mol^{-1}$]) of the R_p^{-1} of the EC elements, obtained by subtracting from E_a (Table 1) the corresponding $E_{a,OV}$ (Figure 1b).

	Fibers	Powders $T < T_{R \rightarrow C\ transition}$	Powders $T > T_{R \rightarrow C\ transition}$
$R_{p,TOT}^{-1}$	115.2	109.0	98.7
$R_{p,RQ1}^{-1}$	–	85.7	84.7
$R_{p,RQ2}^{-1}$	95.9	107.8	108.5
$R_{p,G}^{-1}$	123.2	145.6	–

[–], k_0 is the pre-exponential factor [$Am^{-2}(mol\,m^{-3})^{-v_r - v_p}$], and $E_{a,intrinsic}$ is the intrinsic activation energy of the electrochemical process/EC element. In our case, considering that OVs appear in Reaction (1) and (2), and considering a reaction order of 1 for OVs (and 0 for the other reactants and products)

$$i_0 = C_{OV} k_o \exp\left(-\frac{E_{a,intrinsic}}{RT}\right) \tag{8}$$

Considering that C_{OV} varies exponentially with temperature, as demonstrated in Figure 1b

$$C_{OV} = k_{o,OV} \exp\left(-\frac{E_{a,OV}}{RT}\right) \tag{9}$$

By substituting Equation (9) into Equation (8), the equation below is obtained

$$i_0 = k_o' \exp\left(-\frac{E_{a,intrinsic} + E_{a,OV}}{RT}\right) \tag{10}$$

where $k_0' = k_0\,k_{0,OV}$.

Finally, by substituting Equation (10) into Equation (6)

$$R_p^{-1} = \frac{nFk_o'}{R} \frac{1}{T} \exp\left(-\frac{E_{a,intrinsic} + E_{a,OV}}{RT}\right) \tag{11}$$

Mathematically, the $\left(\frac{1}{T}\right)$ temperature-dependence is practically negligible compared to that of the exponential term. Although some studies also consider the $\left(\frac{1}{T}\right)$ term,[27] usually only the exponential term is retained[17,23]

$$R_p^{-1} = k_o'' \exp\left(-\frac{E_{a,intrinsic} + E_{a,OV}}{RT}\right) = k_o'' \exp\left(-\frac{E_a}{RT}\right) \tag{12}$$

where $k_{0''}$ is again a pre-exponential factor [$\Omega^{-1}\,cm^{-2}$].

Equation (12) provides theoretical support to Equation (5) above. The idea that the overall activation energy E_a is the sum of an intrinsic activation energy ($E_{a,intrinsic}$), plus the formation energy of OVs ($E_{a,OV}$), is similar to what has been proposed for ceria-based oxygen ion conductors, typically employed as electrolytes in IT-SOFCs and SOECs.[28,29] There, the activation energy to ionic conduction is formed of two additive terms, namely the migration enthalpy (H_m) and the association enthalpy (H_a), being the former the energy needed by free vacancies to move through the lattice, and the latter the energy necessary to release vacancies from defect clusters. H_m is $\approx 65\,kJ\,mol^{-1}$, and it is considered independent of dopant identity, which, conversely, strongly affects H_a, usually in the order of tens of $kJ\,mol^{-1}$. At temperatures above $\approx 750\,K$ and in a limited compositional region, almost all the defect clusters would be dissociated and the activation energy to ionic conduction would be roughly equal to the migration enthalpy H_m.

Focusing again on RQ1, Table 3 shows that for powder electrodes $E_{a,intrinsic} \approx 85\,kJ\,mol^{-1}$, independent of crystal structure. With nanofiber electrodes, no RQ1 impedance arc is found. Regarding RQ2, Table 3 shows that for powder electrodes $E_{a,intrinsic} \approx 108\,kJ\,mol^{-1}$, again independent of crystal structure. With nanofiber electrodes, the RQ2 impedance arc is found, and

ChemElectroChem

Research Article
doi.org/10.1002/celc.202500165

**Chemistry
Europe**

European Chemical
Societies Publishing

$E_{a,intrinsic} \approx 96$ kJ mol^{-1}, which is reasonable close to the value found for powders. Therefore, it can be proposed that the RQ2 process in LSCF electrodes has an intrinsic activation energy $E_{a,intrinsic}$ of the order of 102 kJ mol^{-1}, fairly independent of the preparation method and morphology, and independent on the crystal structure.

In principle, the Gerischer element would require a more sophisticated approach, with Equation (6) applied to the electrochemical reaction occurring inside the LSCF material, which should then be coupled to the equations for species transport inside LSCF.[30] These are differential equations requiring numerical solution. Nevertheless, Equation (12) is commonly applied successfully to fit the $R_{p,G}^{-1}$ values obtained from EIS experimental data, as also shown in Figure 3d, and the application of Equation (5) to the Gerischer element can be proposed, albeit in an approximate way. The values of $E_{a,intrinsic}$ are given in Table 3 only for fiber and powder electrodes below the R → C transition, because above the transition the G element vanishes. The values of $E_{a,intrinsic}$ in Table 3 are much closer than the corresponding values of E_a in Table 1. The average value is $E_{a,intrinsic} \approx 134$ kJ mol^{-1}.

4. Conclusions

The role of oxygen vacancies (OVs) in the ORR/OER reaction occurring in La$_{0.6}$Sr$_{0.4}$Co$_{0.2}$Fe$_{0.8}$O$_{3-\delta}$ (LSCF) perovskites has been investigated. Two different LSCF morphologies were tested experimentally: in-house electrospun nanofibers and commercial granular powders. The OV content was evaluated through high-temperature synchrotron XRD. Electrochemistry was tested by means of EIS performed on electrodes prepared in-house with LSCF nanofibers or powders. EIS data were fitted through equivalent circuit modeling. The same equivalent circuit (Rs—RQ1—RQ2—G) was used for both nanofiber and powder electrodes. The attention was focused on the polarization resistance R_p of the individual circuit elements. A clear agreement was found between the variation with temperature of R_p^{-1} and OVs, suggesting that the activation energy of R_p^{-1}, E_a, is the sum of an intrinsic electrochemical activation energy $E_{a,intrinsic}$, plus the formation energy of OVs, $E_{a,OV}$. This holds for all the individual circuit elements. Furthermore, the available data support the assumption that $E_{a,intrinsic} \approx 85$, 102, and 134 kJ mol^{-1} for the R_p^{-1} of the RQ1, RQ2, and G circuit elements respectively, regardless of LSCF preparation route, morphology, and crystal structure. Instead, these strongly influence the formation energy of OVs. According to the results obtained from high-temperature synchrotron XRD, $E_{a,OV} \approx 3$ kJ mol^{-1} for nanofibers, 24 kJ mol^{-1} for powders below the R → C transition, and 0.5 kJ mol^{-1} for powders above the R → C transition.

In conclusion, the results reported in this work lead to the following key findings: 1) The activation energy E_a of the overall polarization resistance of LSCF electrodes includes a significant contribution not related to the electrochemical processes themselves, but instead related to the formation of OVs ($E_{a,OV}$). 2) $E_{a,OV}$ is strongly dependent upon the LSCF preparation route, morphology, and crystal structure. 3) The overall polarization resistances of LSCF electrodes prepared by different synthesis routes or with different morphology or crystal structure exhibit different values of activation energy E_a. 4) Only LSCF synthesis routes characterized by high reproducibility of the preparation process and the resulting electrode morphology are expected to show highly reproducible E_a values. Indeed, electrospinning meets these requirements, and the reproducibility of E_a is confirmed by results reported in the literature by several research groups.

5. Experimental Section

High-Temperature Synchrotron XRD

The structural characterization of the LSCF nanofibers and powders was carried out in air by high temperature synchrotron XRD. Data were collected at 772 K, and then up to 1220 K in steps of about 20 K. Patterns were collected at the XRD1 beamline of the Elettra Synchrotron facility located in Trieste (Italy). Complete description of the experimental procedure was provided in a previous work.[19] The analysis of the diffraction patterns and the refinements through the Rietveld method were performed by the FullProf software.[31] The mathematical analysis made it possible to evaluate the percentage oxygen occupancy in the crystal lattice (O_O). From that, the percentage of oxygen vacancies (V_O) was evaluated as

$$V_O = 100 - O_O \tag{13}$$

Finally, the spatial concentration of oxygen vacancies C_{OV} in the LSCF structure was calculated as

$$C_{OV} = \frac{V_O n_{oxy}}{V_c N_A} \times 100 \left[\frac{kmol}{m^3}\right] \tag{14}$$

where V_O is the percentage of oxygen vacancies, n_{oxy} is the total number of oxygen atoms in the unit cell, V_c is the cell volume in m^3, and N_A is the Avogadro's number.[19]

Electrochemical Impedance Spectroscopy

Electrodes were prepared with both LSCF nanofibers and powders and applied onto Ce$_{0.9}$Gd$_{0.1}$O$_{1.95}$ (gadolinium-doped ceria, GDC) electrolyte circular disks of $\approx 325 \pm 25$ µm thickness and 13 ± 2 mm diameter. ORR/OER characterization was performed using the EIS technique at OCV. During the tests, samples were exposed to a continuous oxygen/argon flow, with p$_{O2} = 0.2$ atm and p$_{Ar} = 0.8$ atm. The spectra were recorded in the frequency range .01 to 1.E6 Hz, with a 10.0 mV voltage amplitude, performing six measurements per decade, using a Gamry Reference 600 potentiostat. For frequencies lower than 1.E5 Hz, the error on the impedance experimental measurements was <1%. For frequencies between 1.E5 and 1.E6 Hz, the experimental error was still <1%, but close to the border of the operating region with error <10%.[32] EIS experimental data were collected at 823 K, and then up to 1223 K in steps of 50 K. To check linearity, stability, and causality, Kramers–Kronig analysis was performed by fitting a generalized model (series of connected Voigt elements) to the spectral data through linear equations.[32,33] This check provided confirmation that the electrode was working in the linear region. Complete description of the experimental procedure was provided in previous works.[16,19,30] The EIS experimental data were fitted through the ECM technique. The equivalent circuit (EC) was a series of four elements
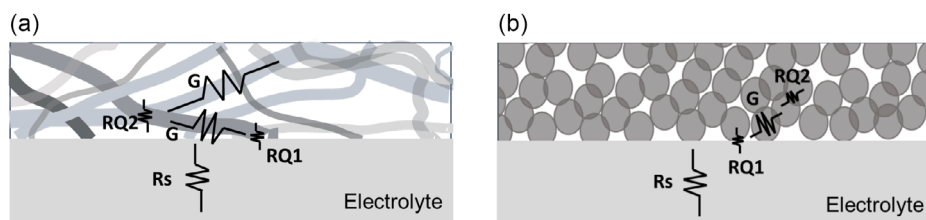
Figure 5. Schematization of the physical significance of the Rs-RQ1-RQ2-G equivalent circuit (EC) for LSCF a) nanofiber and b) powder electrodes.

$$Rs - RQ1 - RQ2 - G \tag{15}$$

with the circuit elements listed in descending order of frequency.[19] The inductance L of the experimental equipment was evaluated separately and subtracted from the experimental data before fitting.

The physical meaning proposed for the EC elements is schematized in **Figure 5** and explained below, together with the mathematical equation of the area–specific impedance Z [$\Omega\,m^2$] as a function of the radial frequency ω [rad s^{-1}].[34]

Rs is the serial resistance associated with the transfer of the oxygen ions through the electrolyte:

$$Z(\omega) = Rel \tag{16}$$

Rel [$\Omega\,cm^2$] being the area–specific resistance of the electrolyte.

RQ1 is associated with the charge transfer between the electrolyte and the electrode, at the interface between the electrolyte and the adjacent nanofibers or granules:

$$Z(\omega) = \frac{1}{R^{-1} + Q(j\omega)^{\alpha}} \tag{17}$$

R [$\Omega\,cm^2$] being here the area-specific resistance of the electrolyte–electrode interface, Q [F cm^{-2} s$^{\alpha-1}$] being the area-specific capacitance of the double layer established at the electrolyte–electrode interface, and α [–] a fitting parameter. From this, the equivalent area-specific capacitance $Q_{equiv.}$ [F cm^{-2}] is defined as follows

$$Q_{equiv} = \frac{(QR)^{\frac{1}{\alpha}}}{R} \tag{18}$$

RQ2 is associated with the charge transfer from one nanofiber to another, or from one granule to another, inside the electrode. Impedance equation as above Equation (18).

G is the Gerischer element, representing the simultaneous charge transfer and electrochemical reaction occurring in the interior of the LSCF nanofibers or granules:

$$Z(\omega) = \frac{1}{Y\sqrt{k + j\omega}} \tag{19}$$

k [s^{-1}] being the oxygen surface exchange coefficient, and Y [Ω^{-1} cm^{-2} s$^{0.5}$] a lumped parameter embedding structural parameters and the solid phase oxygen diffusion coefficient.[17]

At high operating temperatures, one additional element was added to the ECM, namely the finite length Warburg, to fit diffusive limitation effects causing an additional low-frequency impedance arc.[17,19] This is not in the focus of this work and therefore no results are presented. Fittings were performed through Elchemea Analytical.[35]

Given R_p as the area-specific polarization resistance [$\Omega\,cm^2$], an R_p was associated to each EC element. Referring to the Nyquist plots, where each EC element is represented by an arc (Figure 2), R_p was calculated from the fittings as the difference between the low and high frequency intercepts of the impedance arcs with the real axis.[34] For the RQ1 and RQ2 elements, $R_{p,RQ1}$ and $R_{p,RQ2}$ coincide with the R resistance appearing in Equation (17). $R_{p,TOT}$ was the overall electrode polarization resistance

$$R_{p,TOT} = R_{p,RQ1} + R_{p,RQ2} + R_{p,G} \tag{20}$$

In Equation (20), the R_p of Rs, representing the electrolyte, was not included, as well as the R_p of the high-temperature and low-frequency finite length Warburg element.

Conflict of Interest

The authors declare no conflict of interest.

Author Contributions

Paola Costamagna: conceptualization (lead); formal analysis (lead); methodology (equal); visualization (equal); writing—original draft (lead); writing—review and editing (equal). **Caterina Sanna**: investigation (equal); writing—review and editing (equal). **Peter Holtappels**: methodology (equal); writing—review and editing (equal). **Cristina Artini**: conceptualization (equal); resources (equal); writing—review and editing (equal). **Marcella Pani**: conceptualization (equal); resources (equal); visualization (equal); writing—review and editing (equal).

Data Availability Statement

The data that support the findings of this study are available from the corresponding author upon reasonable request.

[1] Q. Ji, L. Bi, J. Zhang, H. Caoa, X. S. Zhao, *Energy Environ. Sci.* **2019**, *13*, 1408.
[2] S. P. Jiang, *Int. J. Hydrogen Energy* **2019**, *44*, 7448.
[3] A. M. Glazer, *Acta Cryst. B.* **1972**, *28*, 3384.
[4] K. S. Aleksandrov, *Kristallografiya* **1976**, *21*, 249.
[5] E. Effori, J. Laurencin, E. Da Rosa Silva, M. Hubert, T. David, M. Petitjean, G. Geneste, L. Dessemond, E. Siebert, *J. Electrochem. Soc.* **2021**, *168*, 044520.
[6] X. Xu, W. Wang, W. Zhou, Z. Shao, *Small Methods* **2018**, *2*, 1800071.
[7] X. Xu, Y. Pan, Y. Zhong, R. Ran, Z. Shao, *Mater. Horiz.* **2020**, *7*, 2519.
[8] E. Bucher, W. Sitte, *J. Electroceram.* **2004**, *13*, 779.
[9] E. Bucher, W. Sitte, G. B. Caraman, V. A. Cherepanov, T. V. Aksenova, M. V. Ananyev, *Solid State Ionics* **2006**, *177*, 3109.
[10] V. A. Cherepanov, LYa Gavrilova, T. V. Aksenova, M. V. Ananyev, E. Bucher, G. Caraman, W. Sitte, V. I. Voronin, *Prog. Solid State Chem.* **2007**, *35*, 175.
[11] B. T. Dalslet, M. Søgaard, H. J. M. Bouwmeester, P. V. Hendriksen, *Solid State Ionics* **2009**, *180*, 1173.
[12] Y. A. Mastrikov, R. Merkle, E. A. Kotomin, M. M. Kukljab, J. Maier, *Phys. Chem. Chem. Phys.* **2013**, *15*, 911.
[13] D. Gryaznov, S. Baumann, E. A. Kotomin, R. Merkle, *J. Phys. Chem. C* **2014**, *118*, 29542.
[14] D. Gryaznov, M. W. Finnis, R. A. Evarestov, J. Maier, *Solid State Ionics* **2014**, *254*, 11.
[15] M. E. Orazem, B. Tribollet, *Electrochemical Impedance Spectroscopy*, John Wiley & Sons, Hoboken, NJ **2017**, p. 389.
[16] P. Costamagna, P. Holtappels, C. Sanna, in *Metal Oxide-Based Nanofibers and Their Applications* (Eds: V. Esposito, D. Marani), Elsevier, Amsterdam **2022**, pp. 301–331, Ch. 13.
[17] P. Costamagna, E. M. Sala, W. Zhang, M. L. Traulsen, P. Holtappels, *Electrochim. Acta* **2019**, *319*, 657.
[18] Y. Chen, Y. Bu, Y. Zhang, R. Yan, D. Ding, B. Zhao, S. Yoo, D. Dang, R. Hu, C. Yang, M. Liu, *Adv. Energy Mater.* **2017**, *7*, 1601890.
[19] M. Daga, C. Sanna, G. Bais, M. Polentarutti, S. Massardo, M. Carnasciali, P. Holtappels, P. Costamagna, M. Pani, C. Artini, *Solid State Ionics* **2024**, *413*, 116620.
[20] D. Chen, Z. Guan, H. Su, W. Yan, C. Liu, H. Li, D. Zhang, W. C. Chueh, *Chem. Mater.* **2024**, *36*, 11635.
[21] T. W. Napporn, Y. Holade, B. Kokoh, S. Mitsushima, K. Mayer, B. Eichberger, V. Hacker, in *Fuel Cells and Hydrogen. From Fundamentals to Applied Research* (Eds: V. Hacker, S. Mitsushima), Elsevier, Amsterdam **2018**, pp. 175–214, Ch. 9.
[22] M. J. Jørgensen, M. Mogensen, *J. Electrochem. Soc.* **2001**, *148*, A433.
[23] V. C. Kournoutis, F. Tietz, S. Bebelis, *Fuel Cells* **2009**, *9*, 852.
[24] S. Ricote, N. Bonanos, F. Lenrick, R. Wallenberg, *J. Power Sources* **2012**, *218*, 313.
[25] A. J. Bard, L. R. Faulkner, in *Electrochemical Methods: Fundamentals and Application*, John Wiley & Sons, NY **2001**, pp. 87–136, Ch. 3.
[26] D. A. Noren, M. A. Hoffman, *J. Power Sources* **2005**, *152*, 175.
[27] A. Szendrei, T. D. Sparks, A. V. Virkar, *J. Electrochem. Soc.* **2017**, *164*, F1543.
[28] B. C. H. Steele, *Solid State Ionics* **2000**, *129*, 95.
[29] C. Artini, S. Presto, M. Viviani, S. Massardo, M. M. Carnasciali, L. Gigli, M. Pani, *J. Energy Chem.* **2021**, *60*, 494.
[30] A. Enrico, P. Costamagna, *J. Power Sources* **2014**, *272*, 1106.
[31] J. Rodriguez-Carvajal, *Phys. B: Condens. Matter* **1993**, *192*, 55.
[32] Gamry Instruments, Reference 620, https://www.gamry.com/potentiostats/reference-620/ (accessed: September 10, 2025).
[33] B. A. Boukamp, *J. Electrochem. Soc.* **1995**, *142*, 1885.
[34] J. R. Macdonald, W. B. Johnson, in *Impedance Spectroscopy: Theory, Experiment, and Applications* (Eds: E. Barsoukov, J. R. Macdonald), John Wiley & Sons, Hoboken, NJ **2018**, pp. 1–20.
[35] S. Koch, C. Graves, K. V. Hansen, Elchemea Analytical **2012**, https://www.elchemea.com (accessed: September 10, 2025).